

Characterization of implanted semiconductors by means of white-beam and plane-wave synchrotron topography

K. Wieteska,^{a*} W. Wierzchowski,^b W. Graeff,^c A. Turos^{b,d} and R. Grötzschel^e

^aInstitute of Atomic Energy, 05-400 Otwock-Swierk, Poland, ^bInstitute of Electronic Materials Technology, Wólczyńska 133, 01-919 Warsaw, Poland, ^cHASYLAB at DESY, Notkestrasse 85, D-22603 Hamburg, Germany, ^dAndrzej Soltan Institute for Nuclear Studies, Hoza 69, 00-681 Warsaw, Poland, and ^eForschungszentrum ROSSENDORF, D-01314 Dresden, Germany. E-mail: e00kw@cx1.cyf.gov.pl

(Received 17 November 1999; accepted 29 June 2000)

$\text{Al}_x\text{Ga}_{1-x}\text{As}$ epitaxial layers, with $x = 0.43$ and GaAs single crystals implanted with various doses of high-energy Se and Si ions, and silicon single crystals implanted with high-energy light ions were studied by means of different X-ray diffraction methods employing either a strongly limited white beam or a highly collimated monochromatic beam. The methods provided complementary characterization of lattice parameter changes and lattice deformation in the implanted layers. The synchrotron rocking curves recorded with a small-diameter beam provided a very good separation of interference maxima and enabled determination of the strain profile. A characteristic difference in strain depth distributions between the implanted $A^{\text{III}}B^{\text{V}}$ compounds and silicon was noticed. Ion implantation in $A^{\text{III}}B^{\text{V}}$ compounds produced a relatively thick layer with an almost constant and distinctly increased lattice parameter in regions close to the surface, whereas, in the case of silicon, shot-through layers with almost unchanged lattice spacing were observed. Other important information obtained from the synchrotron micro-Laue pattern was that the interference fringes caused by crystal curvature or strain gradient are located in the plane of diffraction, while parts of the Laue spot corresponding to the deformed regions are usually displaced.

Keywords: ion implantation; $A^{\text{III}}B^{\text{V}}$ semiconductors; silicon; X-ray diffraction studies; strain profiles.

1. Introduction

Ion implantation is a technique widely used in electronic devices technology. Although it is a subject of extensive studies over several decades, there are still a number of physical phenomena which are not yet well understood. Various X-ray diffraction methods are important tools used for the characterization of implanted layers (e.g. Simon & Authier, 1968; Bonse *et al.*, 1969; Klappe & Fewster, 1994; Ohler *et al.*, 1996, 1997; Wieteska & Wierzchowski, 1995). In recent years there has been considerable interest in studying implanted multicomponent $A^{\text{III}}B^{\text{V}}$ semiconductors (Partyka *et al.*, 1995; Tan *et al.*, 1997; Turkot *et al.*, 1996, 1998).

In the present paper we discuss the application of a set of complementary X-ray methods for investigating two groups of implanted layers differing mainly in their thickness. The first group consisted of a relatively shallow implantation of high-energy Se and Si ions to $\text{Al}_x\text{Ga}_{1-x}\text{As}$ epitaxial layers, while the second category consisted of silicon implanted with high-energy protons and α -particles where the ion ranges were up to ten times larger. The chosen ions are often used in practical application and enable a high-intensity ion beam to be obtained.

Particularly interesting results were obtained by means of methods using a synchrotron white beam limited by a fine slit or a pinhole. The completion of these methods was the recording of rocking curves and plane-wave topographs using synchrotron and conventional multi-crystal X-ray arrangements. The investigated $\text{Al}_x\text{Ga}_{1-x}\text{As}$ epitaxial layers were of high structural perfection and this significantly enhanced observed interference effects. The comparison with silicon seems to be important in view of the different character of the strain depth distribution with a distinct shot-through layer near the surface. A number of new interference phenomena were observed in implanted silicon samples by means of white-beam topographic methods. Partial results of this investigation were presented at the *Highlights in X-ray Synchrotron Investigation*, *SIMC-X* and *X-TOP98* conferences.

2. Experimental

$\text{Al}_x\text{Ga}_{1-x}\text{As}$ epitaxial layers with $x = 0.43$ were grown by the MOCVD method on (001)-oriented GaAs substrates cut out from a Bridgman-grown crystal doped with 0.3%

indium and containing 10^3 cm^{-2} dislocations. The layers were 2.5–3 μm thick and were separated from the substrate by a 0.2 μm -thick undoped GaAs buffer layer. The substrates enabled the growth of layers with similar low-dislocation density, partly due to lower lattice mismatch caused by high indium doping. The value of the lattice parameter in the substrate as determined with the modification of the Bond method described by Godwod *et al.* (1974) was 6.5344 Å. X-ray topographic investigation revealed a very low concentration of misfit dislocations in the samples.

The high-energy ion implantation was performed at room temperature at Rossendorf Research Centre, Dresden, Germany. The $\text{Al}_x\text{Ga}_{1-x}\text{As}$ layers were implanted with 1.5 MeV Se ions in doses in the range 6×10^{13} – 1×10^{15} ions cm^{-2} and with 1 MeV Si ions in doses in the range 1×10^{14} – 2×10^{15} ions cm^{-2} . Implantation energies were chosen to provide a similar penetration range close to 1 μm , when nuclear analysis methods can be used simultaneously. The results for the $A^{\text{III}}B^{\text{V}}$ semiconductors are compared with those obtained using similar X-ray diffraction methods for silicon implanted with 1 MeV and 1.6 MeV protons in doses of 1×10^{17} – 2×10^{17} ions cm^{-2} and with 4.1 MeV α -particles in 1×10^{16} ions cm^{-2} doses. Ion implantation into silicon was performed using a less homogeneous beam than for the $A^{\text{III}}B^{\text{V}}$ samples, producing a lateral dose distribution that can be well approximated by a Gaussian function.

The samples were studied using complementary X-ray methods using both conventional and synchrotron sources of X-rays. The synchrotron investigations were performed with white and monochromatic beam at HASYLAB. The most numerous of the white-beam investigation were performed using the Bragg-case section topographic method (Wieteska *et al.*, 1997a,b, 1998), using a beam limited by a 5 μm narrow slit. The patterns were exposed with a beam entering the samples at a glancing angle of 4–8°.

Bragg-case section topographs recorded at large film-to-crystal distances can provide information on the lattice deformation and its depth location. They can also provide information on the lateral dose distribution along the linear beam. The method is mainly sensitive to changes of orientation but is not directly sensitive to lattice parameter changes. The use of section topography together with the recording of rocking curves is a convenient method for identification of strain relaxation (Wieteska, Wierzchowski, Turos *et al.*, 1997).

In addition to the section experiments, micro-Laue patterns were recorded in a similar geometry using a beam limited by a pinhole with a diameter of 10–30 μm . Here the deformed regions produce mutually displaced spots which may provide information on strain components corresponding to different coordinates. The highly collimated synchrotron beam also significantly enhances diffuse scattering effects with respect to the conventional Laue method.

The synchrotron white-beam experiments were completed by recording rocking curves using multicrystal arrangements both with conventional and synchrotron X-ray sources. The synchrotron arrangement equipped with a two-crystal monochromator and the probe beam limited by a pinhole provided an exact diffraction profile from relatively small areas of diameter 40 μm . Consequently the resolution of subsidiary interference maxima was significantly improved, which was essential for strain-profile analysis based on the fitting of numerically calculated theoretical rocking curves. The small diameter of the probe beam enabled the comparison of rocking curves for different regions of the sample. The intensity of the probe beam and the high resolution of the synchrotron arrangement made it possible to register weak interference maxima located far away from the diffraction peak.

The synchrotron arrangement was also used for recording plane-wave topographs from a 5 mm \times 12 mm area. A very good collimation and high intensity of the beam were essential for revealing the interference fringes corresponding to the subsidiary maxima in rocking curves.

By using a conventional double-crystal diffractometer with Cu $K\alpha_1$ radiation, information on the lattice parameter differences was obtained, allowing the evaluation of strain relaxation. The method consisted of recording three rocking curves for, respectively, a symmetrical 400 reflection and two asymmetrical 511 reflections differing by the rotation about the diffraction vector by 180°. All curves were recorded for the same position of a (111)-oriented Ge monochromator using the 511 reflection. The last two rocking curves corresponded to the glancing angles $\Theta - \varphi$ and $\Theta + \varphi$, respectively, where Θ is the Bragg angle and φ is the inclination of the reflecting plane to the surface.

3. Results and discussion

The most characteristic feature of white-beam Bragg-case section topographs of layered structures is the presence of separated stripes corresponding to the different layers. As shown schematically in Fig. 1, the separation between stripes is caused simultaneously by the different depth of the subsequent layers and by the orientation change of the reflecting planes. These two effects can be separated and evaluated using topographs taken at two different film-to-crystal distances. The separation of the stripes caused by orientation changes increases with the film-to-crystal distance. Contrarily, the separation caused by different depths of the reflecting layers is independent of the film-to-crystal distance. The orientation changes may be revealed only in asymmetric reflections from inclined planes thanks to tetragonal deformation caused by the fitting of layers with different lattice parameters.

The results, which are representative of implanted $\text{Al}_x\text{Ga}_{1-x}\text{As}$ layers with $x = 0.43$, are shown in Fig. 2. The two topographs, covering both implanted and unimplanted areas of the sample implanted with a 1.8×10^{14} ions cm^{-2}

dose of 1 MeV Si ions, were recorded at distances of 15 cm and 30 cm. In the unimplanted area we may note the two stripes corresponding to the epitaxial layer and to the substrate. In the implanted area we note a third distinct and strongly shifted stripe coming from the strained implanted layer. The intensity of the second stripe, corresponding to the epitaxial layer, is much weaker in the implanted area because the damaged layer has consumed a part of the epitaxial layer.

In the two topographs shown in Fig. 2 the displacement of the stripe coming from the implantation increased much more than the separation between two others. This means that the contribution from the depth location is a greater part of the separation of the stripes coming from the layer and the substrate.

In the case of rocking curves for arbitrary asymmetrical reflections, the angular separation between the maximum of the matched thin layer and the maximum of the substrate in rocking curves can be written as

$$\Delta\Theta = \tan\Theta \left\{ \frac{\Delta d}{d} - \left[\sin^2\varphi \left(1 + \frac{2\nu}{1+\nu} \right) - \frac{2\nu}{1+\nu} \right] \xi_{xx} \right\} - \frac{1}{2} \left(1 + \frac{2\nu}{1+\nu} \right) \sin 2\varphi \xi_{xx}, \quad (1)$$

where $\xi_{xx} = \xi_{yy}$ is the in-plane component of the strain tensor, φ is the inclination of the reflecting planes and ν is the Poisson ratio. The first term in the braces describes the contribution from the lattice parameter difference modified by the tetragonal deformation of the lattice. It should be pointed out that only the last term describing an additional misorientation of the lattice $\Delta\varphi$, caused by the tetragonal deformation, is responsible for the effects recorded in white-beam section topographs. It is easily visible that the displacement of the stripes in the section pattern perpendicular to the incident beam may be written as

$$\Delta z = (2\Delta\varphi_T d_{fc} \cos 2\Theta + \Delta t) \cos\phi, \quad (2)$$

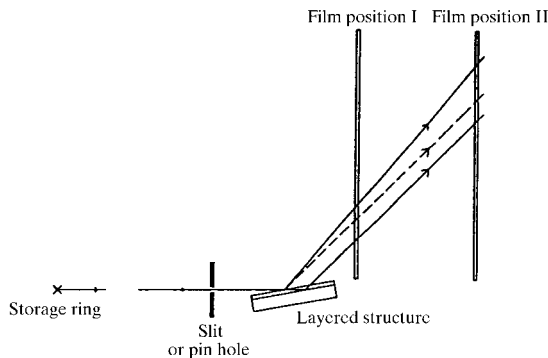


Figure 1

Scheme for separating the depth location and deformation effects in Bragg-case section topographs of layered structures. The dashed line represents the propagation of the effect coming from a different depth location, while the upper solid line represents the propagation of a common effect of deformation and depth location.

where d_{fc} denotes the film-to-crystal distance, Δt is the contribution of the depth location effects and ϕ is the azimuthal coordinate of the Laue spot in the plane of the film. As measured from the topographs in Fig. 2, the contribution due to the misorientation is equal to $160''$, while the displacement Δt is smaller than $2\ \mu\text{m}$. From equation (2) one can evaluate the lattice parameter change as 4×10^{-4} .

The value of the strain ξ_{xx} and the disorientation $\Delta\varphi$ in the implanted and epitaxial layers can be obtained from three rocking curves for reflections with different asymmetry shown in Fig. 3, due to the fact that the last term in (1) changes its sign with φ . These curves can also be used for evaluation of the strain relaxation and for evaluation of the Poisson ratio ν . The lattice parameter difference was found to be 4×10^{-4} and the value of the Poisson coefficient was found to be 0.32.

The lattice parameter difference $\Delta d/d$ can be obtained from the rocking curve for the symmetrical reflection. The method using three curves can independently provide information about the lattice parameter difference and the degree of relaxation in the sample.

The important difference between the Bragg-case section topographs for $A^{\text{III}}B^{\text{V}}$ compounds implanted with Se and Si ions and silicon implanted with high-energy light ions concerns the visibility of the deformation effect, which is very weak in the second case. This can be observed in Fig. 4, which shows the section topographs for proton-implanted silicon taken at a large (50 cm) film-to-crystal distance. The main part of the image is formed by stripes coming from the upper part of the surface, two flanks of the mostly damaged region and the substrate (Wieteska *et al.*, 1998). In the present case the increase of the film-to-crystal distance essentially caused the diffusion of these stripes due to the decrease of the spatial resolution. In addition, in

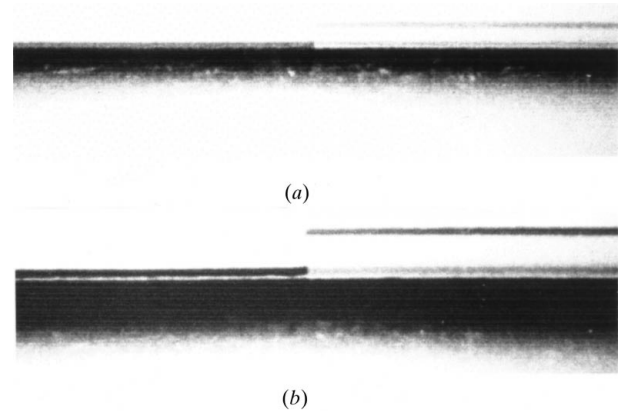


Figure 2

White-beam Bragg-case section topographs in 115 reflection selecting $0.77\ \text{\AA}$ radiation of an $\text{Al}_x\text{Ga}_{1-x}\text{As}/\text{GaAs}$ epitaxial layer with $x = 0.43$ implanted with a dose of $1.8 \times 10^{14}\ \text{ions cm}^{-2}$ of 1 MeV Si ions taken at film-to-crystal distances of (a) 15 cm and (b) 30 cm. The left part of the topographs is covering the unimplanted part of the layer. The horizontal width of the picture covers 7 mm.

some highly exposed spots we observe a shadow corresponding to the ion dose distribution, which is visible in the upper part of both topographs in Fig. 4.

Our latest Bragg-case section investigation of implanted $A^{III}B^V$ compounds (Wieteska, Wierzchowski, Graeff *et al.*, 1999) revealed that, in the presence of shot-through layers, when the strain reached its maximum at a certain depth, the stripe corresponding to the implanted layer transforms into a series of interference fringes. This phenomenon is due to the interference of X-rays diffracted by the layers with similar tetragonal deformation situated on both sides of the

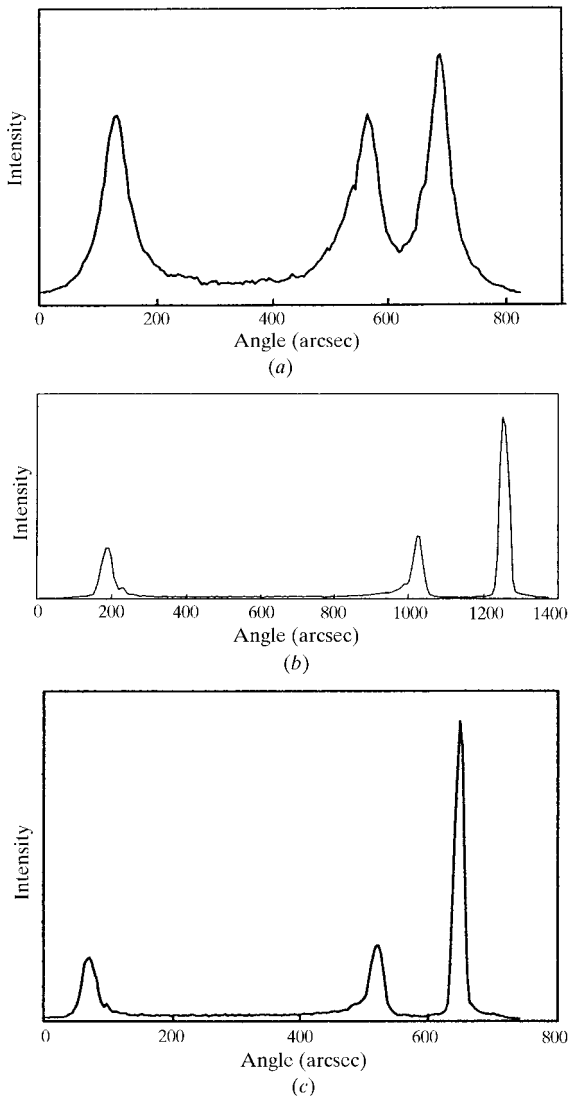


Figure 3

Three rocking curves enabling evaluation of strain relaxation, taken with $\text{Cu } K\alpha_1$ radiation in double-crystal arrangements with a 511 Ge monochromator. (a) For symmetrical 400 reflection (nonparallel setting). (b) and (c) Two asymmetrical reflections with glancing angles $\Theta + \varphi$ for an $\text{Al}_x\text{Ga}_{1-x}\text{As}/\text{GaAs}$ epitaxial layer with $x = 0.43$ implanted with a dose of 1.8×10^{14} ions cm^{-2} of 1.5 MeV Se ions. In all three curves (a–c) the corresponding peaks from left to right are: from the implanted layer, from the non-penetrated part of the epitaxial layer, and from the substrate.

strain maximum and will be discussed in detail in a forthcoming paper. Traces of such fringes can be seen in the pattern shown in Fig. 4(b).

Other important elements of the section pattern of the proton-implanted silicon sample in Fig. 4(a) are contrasts located in the lower part of the image, which are probably deformed interference fringes. These fringes are most probably formed by a deformation gradient, as in elastically bent crystals. The fringes become distinctly stronger in the implanted area and sometimes form a series, suggesting multiple reflection of the radiation inside the crystal.

Similar interference fringes were observed for an implanted bent silicon crystal shown in Fig. 5. The formation mechanism of these fringes (Chukhovskii & Petrashen, 1988) assumes the redirection of the wave-field trajectories in the bent crystals and their reflection by the surface. The Bragg-case section pattern for the implanted region usually contains more complicated and distinct fringe patterns than for the unimplanted region. This is most probably caused by the interference effects between the wave fields in the undisturbed bent surface and the shot-through layer for which the dispersion surface is not very much displaced with respect to that for the substrate. The character of the interference effects in the implanted regions was well reproduced by the numerical simulation based on the Takagi-Taupin theory as shown in Fig. 5(b). The simulation assumed a two-dimensional distribution of the ion dose described by the top part of the Gaussian curve. In the case of bent implanted crystals, a kind of echo was sometimes observed, which is most probably formed by the increased intensity of the beam reflected towards the bent substrate (Wieteska *et al.*, 1997b).

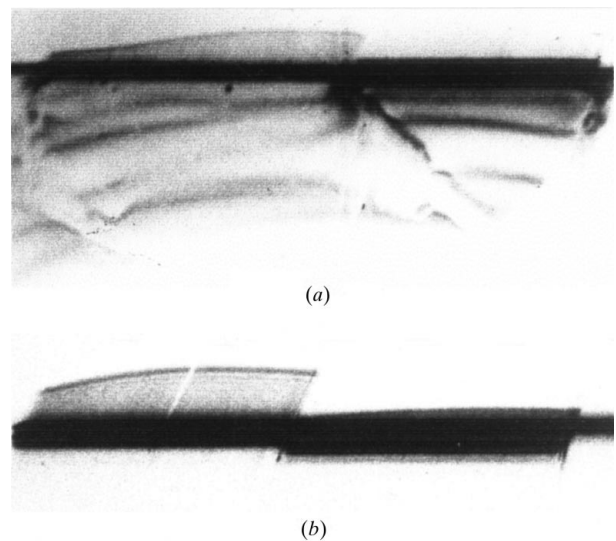


Figure 4

Bragg-case section topographs taken at large (50 cm) film-to-crystal distances for the silicon sample implanted with 1.6 MeV (right) and 1 MeV protons (left) with a dose of 1×10^{17} ions cm^{-2} of negligible curvature taken for (a) 242 reflection of 0.8 Å radiation and (b) 10,6,4 reflection of 0.36 Å radiation. The horizontal widths of the pictures are 7 mm.

One notices a certain analogy of the above-described echo and weak interference fringes in the previously described flat proton sample. For this reason one can expect an analogous mechanism responsible for these effects. The most probable reason for wave-field redirection in the proton-implanted sample is small lattice parameter gradients which, as is well known from the dynamical theory, cause similar effects as lattice bending. A large thickness of the sample increases the intensity of the effects caused by strain gradients. Owing to a very high absorption of the second wave field, the visibility of the interference fringes caused by bending or strain gradients is usually much weaker in the case of $A^{III}B^V$ compounds.

The micro-Laue patterns shown in Fig. 6 indicate that the above-discussed interference effects are formed by the radiation leaving the crystal in the plane of diffraction of the substrate. Contrarily, the radiation forming the dose-dependent shadow visible in Fig. 4 corresponds to the rotation of the diffraction vector about the intersection of the reflecting plane with the surface of the sample, as predicted by the assumed model of deformation (Wieteska *et al.*, 1998; Wieteska, Wierzchowski & Graeff, 1999). This can be observed in Fig. 6(a). In different reflections the direction of the streak is varying and hence the characteristic shadow may be located either on the upper or the lower side of the main set of stripes in the section image.

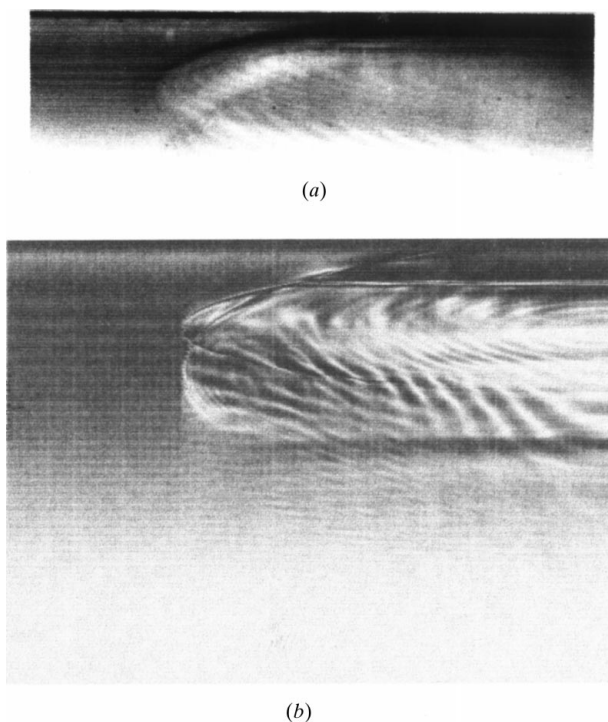


Figure 5

Bragg-case section topograph of an elastically bent silicon crystal implanted with a dose of $1 \times 10^{16} \text{ cm}^{-2}$ of 4.1 MeV α -particles taken for (a) the 111 reflection selecting 0.7 Å radiation and (b) the corresponding simulation obtained by numerical integration of the Takagi-Taupin equations.

As shown in Fig. 6(d), the implanted $A^{III}B^V$ layers, for which the section pattern contains three separate stripes, produce three separate micro-Laue spots displaced in the same manner as strokes corresponding to the dose-dependent shadow in Fig. 6(a).

The described differences between the section and micro-Laue pattern for the two groups of presently investigated implanted layers correspond to the different character of their rocking curves. In the case of silicon implanted with high-energy protons the upper shot-through layer contributes either to the maximum produced by the substrate or, at high doses, produces a high peak situated very close to that of the substrate. This can be followed in Fig. 7. The deformed region situated below the shot-through layer produces a long tail of interference maxima with periodicity significantly increasing towards the low angles. It was found that the maximum situated at the lowest angle corresponded to the mostly deformed regions. It is often slightly higher than neighbouring ones. The curves recorded with a synchrotron arrangement contain a very large number of maxima, up to 50 or more. As has already been shown in Fig. 3, the implantation of

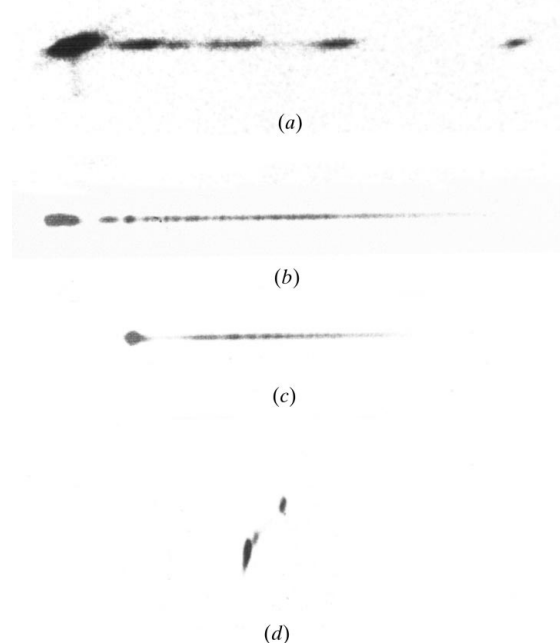


Figure 6

Comparison of micro-Laue spots for different implanted silicon samples and $\text{Al}_x\text{Ga}_{1-x}\text{As}$ samples. (a) For the 14,4,2 reflection using 0.17 Å radiation in the same sample as in Fig. 4. (b) For implanted and (c) non-implanted areas of the same bent silicon sample as in Fig. 5 taken for the 335 reflection using 0.65 Å radiation. (d) For $\text{Al}_x\text{Ga}_{1-x}\text{As}$ implanted with a dose of $2 \times 10^{14} \text{ cm}^{-2}$ of 1.5 MeV Se ions in the 206 reflection using 0.55 Å radiation. In the complete Laue pattern the long tails of the spot shown in (a), (b) and (c), as well as the lowest most-intensive fragment of spot in (d), point towards the intersection of the incident beam with the film proving that they are formed by the radiation located in the plane of diffraction. Magnification: $\times 20$.

$A^{III}B^V$ compounds with heavy ions usually produces a distinct maximum situated at low angles and followed by the interference maxima situated only at higher angles. With increasing doses this maximum usually becomes higher and more distinct. This maximum was strongly separated from that of the substrate and from that due to the non-penetrated epitaxial layer.

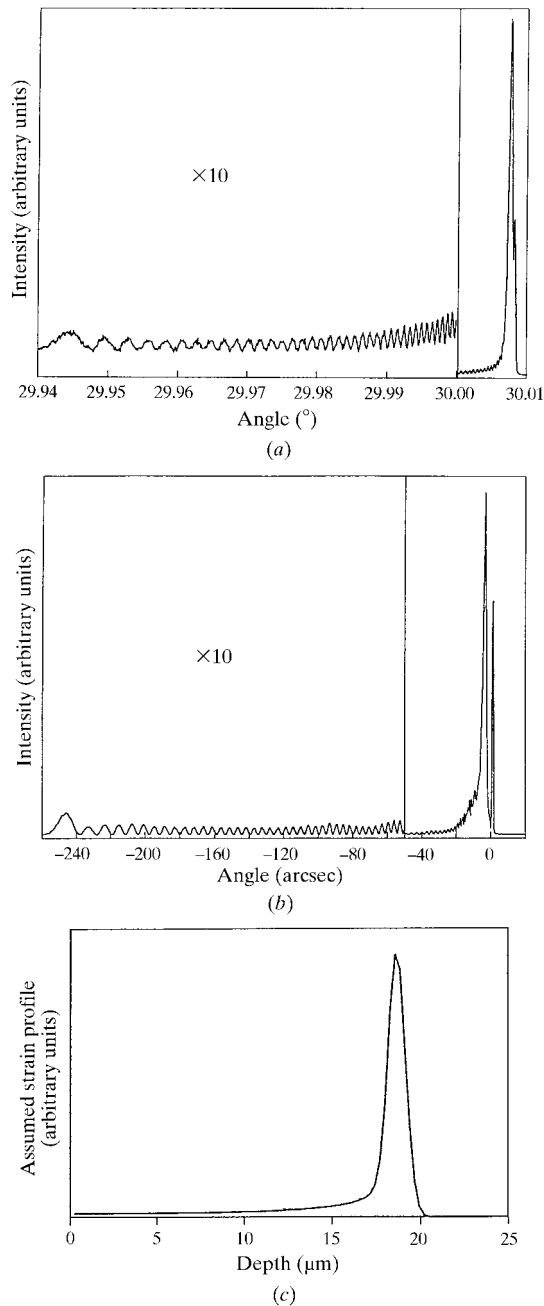


Figure 7
(a) The synchrotron rocking curve in symmetrical 111 reflection using 1.1 Å radiation for silicon implanted with a dose of $1 \times 10^{17} \text{ cm}^{-2}$ of 1.5 MeV protons. (b) The theoretical rocking curve obtained by numerical integration of the Takagi-Taupin equations corresponding to (a). (c) The assumed strain profile equal to the vacancy distribution calculated using *TRIM-95* used for computation of curve (b).

The presently recorded symmetrical synchrotron rocking curves were crucial for the determination of strain profiles. The experimental rocking curves and fitted theoretical curves as well as the assumed strain profiles are shown in Figs. 7 and 8. In the case of silicon

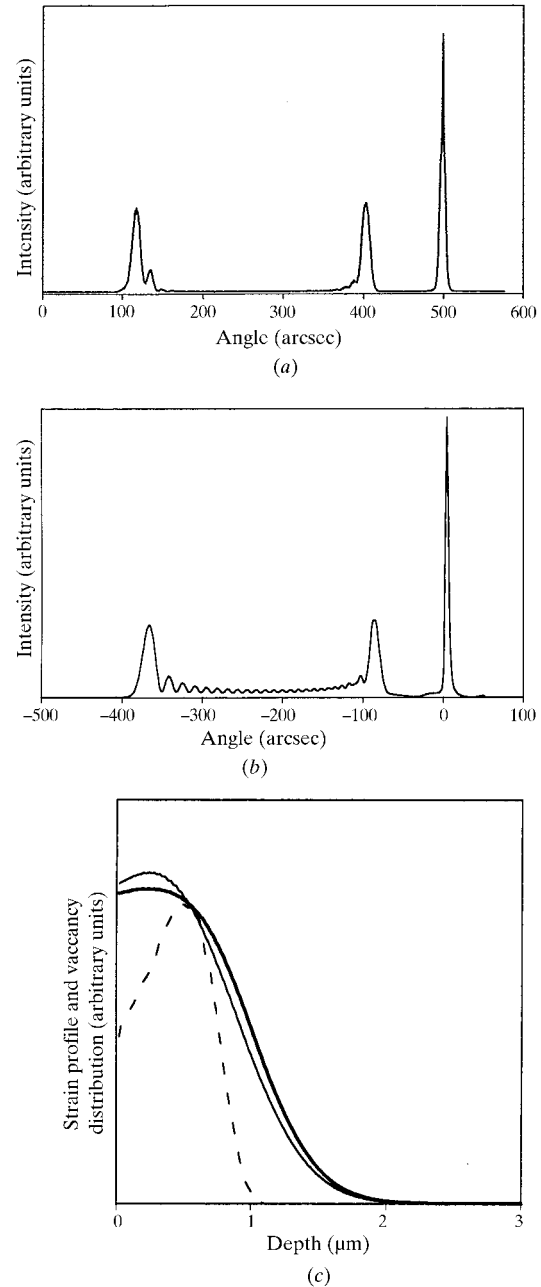


Figure 8
(a) Synchrotron rocking curve in symmetrical 400 reflection using 1.1 Å radiation for highly perfect $\text{Al}_x\text{Ga}_{1-x}\text{As}/\text{GaAs}$ epitaxial layers with $x = 0.43$ implanted with a dose of $2 \times 10^{14} \text{ ions cm}^{-2}$ of 1.5 MeV Se ions. (b) The theoretical rocking curve obtained by numerical integration of the Takagi-Taupin equations corresponding to (a). (c) Calculation of the strain profile used for computation of curve (b): the three curves denoted by the thin, dashed and thick lines correspond to, respectively, the initial *TRIM-95* vacancy profile, its transformation by diffusion, and the final profile obtained assuming the saturation is dependent on the local vacancy concentration approximated by a sine function.

implanted with protons and α -particles, an adequate approximation of the strain profile was provided by the vacancy distribution calculated using the *TRIM-95* program (Ziegler *et al.*, 1985). In particular, this approximation allowed reproduction of a rocking curve with more than 50 subsidiary maxima for high-dose proton-implanted silicon (Wieteska *et al.*, 1998) and the interference fringes in plane-wave topographs.

A different situation was observed for the studied implanted $\text{Al}_x\text{Ga}_{1-x}\text{As}$ layers, where the approximation of strains by vacancy distribution profiles did not produce an adequately high maximum. The suitable strain profile was obtained arbitrarily assuming a two-step mechanism. In the first step the vacancy profile obtained from *TRIM-95* was transformed by numerically solving the diffusion equation. In the second step the profile was modified by taking the sine function, which is a good approximation of the macroscopic dependence of lattice parameter change on the dose.

Assuming an increase in the height of the initial vacancy profile and the diffusion range with increasing dose, a good agreement of the theoretical rocking curves with the experimental synchrotron and conventional rocking curves for a range of samples implanted with different doses was obtained (Wierzchowski, Wieteska, Graeff, Turos & Grötzel, 1999; Wierzchowski, Wieteska, Graeff & Turos, 1999). The shape of the final strain distribution was, to a great extent, confirmed by

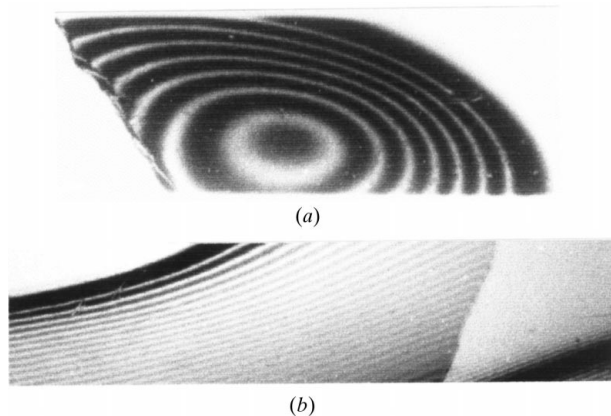


Figure 9

(a) A representative synchrotron plane-wave topograph for an unimplanted silicon sample implanted with an average dose of 1×10^{17} ions cm^{-2} of 1 MeV protons. All points of the topograph correspond to the same angular difference from the substrate maximum, and the observed fringes correspond to the dose changes resulting in different positions of subsidiary interference maxima. (b) A representative synchrotron plane-wave topograph for $\text{Al}_x\text{Ga}_{1-x}\text{As}/\text{GaAs}$ epitaxial layers with $x = 0.43$ implanted with a dose of 2.4×10^{14} ions cm^{-2} of 1.5 MeV Se ions. The left-hand side corresponds to the implanted area and the strongest black stripe in the upper part corresponds to the implanted layer maximum. The strong stripe on the lower right-hand side is due to the epitaxial layer peak in the non-implanted region. The horizontal widths of the images are approximately 7 mm.

Rutherford backscattering experiments which will be published separately.

Bending of studied $\text{Al}_x\text{Ga}_{1-x}\text{As}$ layers resulted in obtaining fringes in the double-crystal topograph, corresponding to passing the different subsidiary maxima in the rocking curve as illustrated in Fig. 9(a). In the case of the presently studied silicon crystals, the appearance of fringes is, to a greater extent, caused by inhomogeneity of the bombarding beam (Fig. 9b).

4. Conclusions

The complementary use of white-beam methods with a limited beam and multicrystal arrangement provides effective means of measuring lattice parameter changes, lattice deformation and depth location of different layers in implanted epitaxial layers and single crystals.

The important result obtained using different X-ray methods is the lack of separate diffraction peaks in the case of silicon implanted with light ions which are well visible in the case of $A^{\text{III}}B^{\text{V}}$ compounds implanted with Si and Se ions.

It was found that the vacancy distribution profile is a good approximation of the lattice parameter change distribution in silicon. In the case of $A^{\text{III}}B^{\text{V}}$ compounds, suitable strain profiles were obtained from the vacancy profile assuming diffusion and saturation, forming a layer with almost constant lattice parameter in the near-surface region.

The authors are indebted for the financial support from the State Committee for Scientific Research (grant 8 T11B 049 13) and from the Polish-German Agreement on Cooperation POL-GER-N-100-95/BO (204/P-3).

References

- Bonse, U., Hart, M. & Schwuttke, G. H. (1969). *Phys. Status Solidi*, **33**, 361–374.
- Chukhovskii, F. & Petrashen, P. V. (1988). *Acta Cryst.* **A44**, 8–14.
- Godwod, K., Kowalczyk, R. & Szmigiel, Z. (1974). *Phys. Status Solidi*, **A21**, 227–233.
- Klappe, J. G. & Fewster, P. F. (1994). *J. Appl. Cryst.* **27**, 103–110.
- Ohler, M., Härtwig, J. & Prieur, E. (1997). *Acta Cryst.* **A53**, 199–201.
- Ohler, M., Prieur, E. & Härtwig, J. (1996). *J. Appl. Cryst.* **29**, 568–573.
- Partyka, P., Averbach, R. S., Coleman, J. J., Erhart, P. & Jäger, W. (1995). *Mater. Res. Soc. Symp. Proc.* **354**, 219–224.
- Simon, D. & Authier, A. (1968). *Acta Cryst.* **A24**, 527–534.
- Tan, H. H., Jagadish, C., Williams, J. S., Zou, J., Cockayne, D. H. J. & Sikorski, A. (1997). *J. Appl. Phys.* **77**, 87–94.
- Turkot, B. A., Lagow, W., Robertson, I. M., Forbes, D. V., Coleman, J. J., Rehn, L. E. & Baldo, P. M. (1996). *J. Appl. Phys.* **80**, 4366–4372.
- Turkot, B. A., Robertson, I. M., Rehn, L. E., Baldo, P. M., Forbes, D. V. & Coleman, J. J. (1998). *J. Appl. Phys.* **83**, 2539–2547.

- Wierzchowski, W., Wieteska, K., Graeff, W. & Turos, A. (1999). *J. Alloys Compd.* **286**, 343–348.
- Wierzchowski, W., Wieteska, K., Graeff, W., Turos, A. & Grötzschel, R. (1999). *IEEE Conf. Ser. (SIMC-X)*, pp. 181–184.
- Wieteska, K. & Wierzchowski, W. (1995). *Phys. Status Solidi A*, **147**, 55–66.
- Wieteska, K., Wierzchowski, W. & Graeff, W. (1997a). *Il Nuovo Cimento*, **19D**, 233–239.
- Wieteska, K., Wierzchowski, W. & Graeff, W. (1997b). *J. Appl. Cryst.* **30**, 238–243.
- Wieteska, K., Wierzchowski, W. & Graeff, W. (1999). *J. Alloys Compd.* **286**, 349–353.
- Wieteska, K., Wierzchowski, W., Graeff, W. & Dlużewska, K. (1998). *Phys. Status Solidi A*, **168**, 11–25.
- Wieteska, K., Wierzchowski, W., Graeff, W., Turos, A., Gawlik, G. & Grötzschel, R. (1999). XVIIIth International Union of Crystallography Congress, 4–13 August 1999, Glasgow, UK. Abstract No. PO6.11.018.
- Wieteska, K., Wierzchowski, W., Turos, A., Graeff, W. & Grötzschel, R. (1997). *Universitatis Iagiellonicae Folia Physica, Fas. XXXIX*, pp. 85–90.
- Ziegler, J. F., Biersack, J. P. & Litmark, U. (1985). In *The Sopping and Range of Ions in Solids*, edited by J. F. Ziegler. New York: Pergamon Press.